Journal of Materials Chemistry C

Chemical Vapor Deposition and Phase Stability of Pyrite on SiO_2

Journal:	*Journal of Materials Chemistry C*
Manuscript ID	TC-ART-02-2018-000584.R1
Article Type:	Paper
Date Submitted by the Author:	02-Apr-2018
Complete List of Authors:	Mutlu, Zafer; University of California, Materials Science and Engineering Debnath, Bishwajit; Univ Calif Riverside, Mechanical Engineering Su, Shanshan; University of California, Riverside Li, Changling; University of California, Materials Science and Engineering; Applied Materials Inc, DSM Ozkan, Mihri; University of California Riverside, Department of Electrical Engineering Bozhilov, Krassimirt; University of California, Riverside, Central Facility for Advanced Microscopy and Microanalysis, Materials Science and Engineering Program Lake, Roger; Laboratory for Terahertz and Terascale Electronics (LATTE), Dept. of Electrical and Computer Engineering, University of California Riverside Ozkan, Cengiz; Univ Calif Riverside, Mechanical Engineering

Journal Name

ARTICLE

Chemical Vapor Deposition and Phase Stability of Pyrite on SiO_2

Z. Mutlu[a,b], B. Debnath[b], S. Su[b], C. Li[a], M. Ozkan[b], K. N. Bozhilov[c], R. K. Lake[b], and C. S. Ozkan[a,d,*]

Received 00th January 20xx,
Accepted 00th January 20xx

DOI: 10.1039/x0xx00000x

www.rsc.org/

Semiconducting pyrite (cubic-FeS_2) is of great interest for photovoltaics, energy-storage and catalysis applications due its remarkable optical, electrochemical and catalytic properties in combination with its high abundance, low raw material cost and environmental benignancy. In addition, recent theoretical studies indicate that it is possible to synthesize two-dimensional (2D) FeS_2 with atomic thickness, and 2D FeS_2 possess highly tunable electronic and magnetic properties that do not exist in its bulk form, enabling its application in nanoelectronics. Herein, we report the first growth of single-phase FeS_2 on SiO_2 substrates at temperatures between 300 C and 600 C by atmospheric pressure chemical vapor deposition (CVD). The temperature-dependent growth studies suggest that air-stable FeS_2 crystals with 2D morphologies grow at 450 C and above while smaller irregular-shaped FeS_2 with low crystallinity and poor stability form at lower temperatures. We also demonstrate the patterned growth of 2D hexagonal crystals on SiO_2 substrates using graphene as a template at 600 C. Raman spectroscopy measurements in conjunction with *ab-initio* density functional theory (DFT) calculations confirm that the growth up to 600 C does not include any other phase than FeS_2. Moreover, we show that laser-induced local phase transformations from FeS_2 (pyrite phase) and FeS (troilite phase) can be monitored in-situ by the changes in Raman spectra. Our method paves the way toward scalable synthesis of phase-pure FeS_2 crystals on SiO_2 substrates, which is fully compatible with semiconductor processing. This method can be also further developed and adopted for the synthesis of atomically thin 2D FeS_2 layers and their heterostructures with graphene that may bring enhanced or novel properties.

Introduction

Iron sulfides constitute a diverse group of compounds containing iron (Fe) and sulfur (S) elements. These sulfides can exist in a variety of phases by depending on the stoichiometric ratios and oxidation states of Fe and S. The most well-known examples of iron sulfide phases include pyrite (cubic-FeS_2), marcasite (orthorhombic-FeS_2), greigite (Fe_3S_4), pyrrhotite ($Fe_{1-x}S$), troilite (FeS), and mackinawite ($Fe_{1+x}S$). Amongst these phases, pyrite is the most stable and abundant phase. Pyrite crystallizes in a cubic structure with a space group symmetry of $Pa\overline{3}$. The Fe atoms occupy the sites of a face-centered cubic (fcc) sublattice, and the S atoms are placed in the form of S-S dumbbells aligned along the cube diagonal direction ⟨111⟩. Each Fe atom is octahedrally coordinated by six nearest-neighbor S atoms in a slightly distorted octahedron, and each S atom is coordinated to three Fe and one S atom in a distorted tetrahedron configuration. The pyrite structure is fully characterized by the lattice constant a=5.416 Å and the Wyckoff parameter x=0.385 Å.[1-3]

With its combination of suitable energy band gap (E_g = 0.80–0.95 eV), large absorption coefficient (α~ 6 x 10^5 cm^{-1} for hυ > 1.3 eV), long minority carrier diffusion length (100-1000 nm), high stability, environmental compatibility, high abundance, and low raw material cost, pyrite has received a great deal of attention over the past decades as a promising material for photovoltaic applications.[4-6] However, despite extensive research efforts, the solar conversion efficiency of pyrite has remained below 3%. Cabán-Acevedo et al.[4] have recently shown that the low solar conversion efficiency of pyrite single crystals can be mainly attributed to the presence of intrinsic bulk deep donor states in high density, likely resulting from by bulk sulfur vacancies.

Due to its high abundance, low raw material cost, non-toxicity, and high theoretical specific capacity (894 $mAhg^{-1}$)[7], pyrite has been also recognized as a highly promising cathode material in lithium-ion batteries (LIBs). However, the development of LIBs with pyrite cathodes has been hampered by unsatisfied rate ability and low capacity retention, and continuous reversible capacity fading due to the poor conductivity, large volume change, and shuttling effect[8]. It has been reported that the morphology of pyrite plays an important role in alleviating some of these issues raised by its use in LIBs. For instance, Li et al.[9] showed that the use of pyrite in the form of nanowires as cathodes in LIBs improve the reaction kinetics by shortening the Li+ and electron transport path, which leads to the high capacity and excellent capacity retention.

The ability to tailor materials properties by nanostructuring has become one of the foundations of modern materials

[a] Materials Science and Engineering Program, University of California, Riverside, CA 92521, USA.
[b] Department of Electrical and Computer Engineering, University of California, Riverside, CA 92521, USA.
[c] Central Facility for Microscopy and Microanalysis, University of California, Riverside, CA 92521, USA.
[d] Department of Mechanical Engineering, University of California, Riverside, CA 92521, USA.
*E-mail: cozkan@engr.ucr.edu

science. Several pyrite nanostructures with different morphologies have been reported.[10,11] Examples include, but not limited, zero-dimensional (0D) nanoparticles[12], one-dimensional (1D) nanowires[13], two-dimensional (2D) hexagonal sheets[14], and three-dimensional (3D) nanocubes[15]. Recent experimental and theoretical studies[14,16,17] have shown that 2D confinement in pyrite can remarkably enhance its optical, electronic, magnetic, electrocatalytic, and electrochemical properties compared to their bulk counterparts due to nanoscale effects. Kirkeminde et al.[14] demonstrated that 2D pyrite nanoplates show great promise for the fabrication of hybrid bulk heterojunction solar cells. Jasion et al.[16] showed that 2D pyrite nanostructures exhibit a better electrocatalytic performance than 1D wires and 3D cubes under neutral pH conditions, due to a high specific surface area and maximized surface active sites. Zhang et al.[18] and Yakovkin et al.[19] proposed that 2D pyrite exhibits mechanical-strain tunable magnetism and thickness tunable band gap while the bulk pyrite does not possess any magnetism and band gap tunability. 2D pyrite with tunable electronic and magnetic properties has potential for nanoelectronics and nanomagnetics applications, which will require pyrite to be supported by a substrate, such as SiO_2.

The rich phase chemistry of iron sulfides presents a challenge to synthesis. A variety of synthesis methods have been reported for the synthesis of pyrite nanostructures; some of recent notable examples include solvothermal process[20], solution-phase deposition[23], thermal sulfidation[11,17] and chemical vapor deposition (CVD)[25,26]. Morphology controlled pyrite nanoparticles were obtained by the solution-based processing and preparation techniques[20,22-24]. However, post treatment is generally required to remove any residual organics and to improve the particle size and crystallinity for the device applications[5]. Cabán-Acevedo et al.[11] demonstrated the synthesis of single crystal pyrite nanostructures with different morphologies by the thermal sulfidation and studied their electrical properties. This method provides the pyrite nanostructures that can potentially serve as an ideal platform for fundamental research; however, it is not suitable for large-scale device production in its current stage. Berryet al.[25] demonstrated the synthesis of the pyrite thin films on glass and molybdenum-coated glass substrates by atmospheric-pressure CVD using iron(III) acetylacetonate and tert -butyl disulfide as Fe and S precursors. While this method enables the large-scale scalable production, the synthesized films have high resistivity and low mobility.

Herein, for the first time, we grew phase-pure pyrite crystals on SiO_2 and graphene/SiO_2 substrates by atmospheric pressure chemical vapor deposition (CVD) method using S and iron (III) chloride ($FeCl_3$) powder as S and Fe precursors, respectively. We systematically investigated the effect of the growth temperature on the crystallinity, morphology, and phase stability of the crystals. Furthermore, the phase stability of the crystals and possible phase transformations were studied as a function of laser irradiation power by in-situ Raman spectroscopy.

Methods

Materials synthesis

In a typical CVD process, a Si substrate with a 285 nm SiO_2 capping layer was placed facing down on an alumina crucible containing $FeCl_3$ powder (~ 0.1 mg) and put in the middle of a quartz tube. $FeCl_3$ was selected due to its high partial pressure and transport rate that promotes the growth of large planar crystals.[6] S powder (~ 1 gr) were loaded in a small quartz tube with a tiny hole for uniform evaporation and located at upstream of the quartz tube (**Figure 1a**). The pyrite crystals were obtained on the SiO_2 substrate by heating the furnace to 300 C, 450 C, and 600 C at a rate of 20 C/min and held at these temperatures for 60 min before cooling down to room temperature naturally. All growth experiments were performed under atmospheric pressure with an argon (Ar) flow of 100 sccm inside a fume hood.

The same recipe was used for the growth of the pyrite crystals on SiO_2 substrates using graphene islands as growth template at 600 C. Details of the graphene growth and subsequent transfer onto the SiO_2/Si substrates are given in our recent work[29].

Materials characterization

Raman spectroscopy was performed on a Horiba LabRam HR instrument equipped with a 523-nm laser supply and an 1800 lines/mm grating. A 100x objective was used for focusing the laser to an approximately 0.8 μm spot onto the sample. The laser power was kept below 1 mW to prevent sample heating.

X-ray photoelectron spectroscopy (XPS) characterization was carried out by using a Kratos AXIS ULTRADLD XPS system equipped with an Al Kα monochromated X-ray source and a 165-mm mean radius electron energy hemispherical analyser. The vacuum pressure was kept below $3x10^{-9}$ torr, and the neutralizer was applied during the data acquisition.

Scanning electron microscopy (SEM) imaging, energy-dispersive X-ray spectroscopy (EDS) analysis, and electron backscatter diffraction (EBSD) measurements were performed on an FEI NNS450-FEG SEM equipped with an in-lens secondary electron/backscattered electron (SE/BSE) detector (TLD), an EDX detector 50 mm^2 X-Max50 SDD with a resolution of 127 eV at Mn Kα, and an EBSD NORDLYS Nano CCD camera detector, respectively. SEM, EDS and EBSD measurements were carried out using an accelerating voltage of 5 keV, 15 kEV and 20 keV, respectively. XPS spectra were deconvoluted to the components using Gaussian function after a Shirley[30] background subtraction. The XPS spectra were calibrated to the position of C sp^2 peak of 284.6 eV.

Angle-resolved polarized Raman spectroscopy (ARPRS) was performed on a Renishaw inVia Raman microscope equipped with a 488-nm laser supply and a 1200 lines/mm grating. A 50x objective was used for focusing the laser to an approximately 0.8 μm spot onto the sample. The laser power was kept below 1 mW to prevent sample heating.

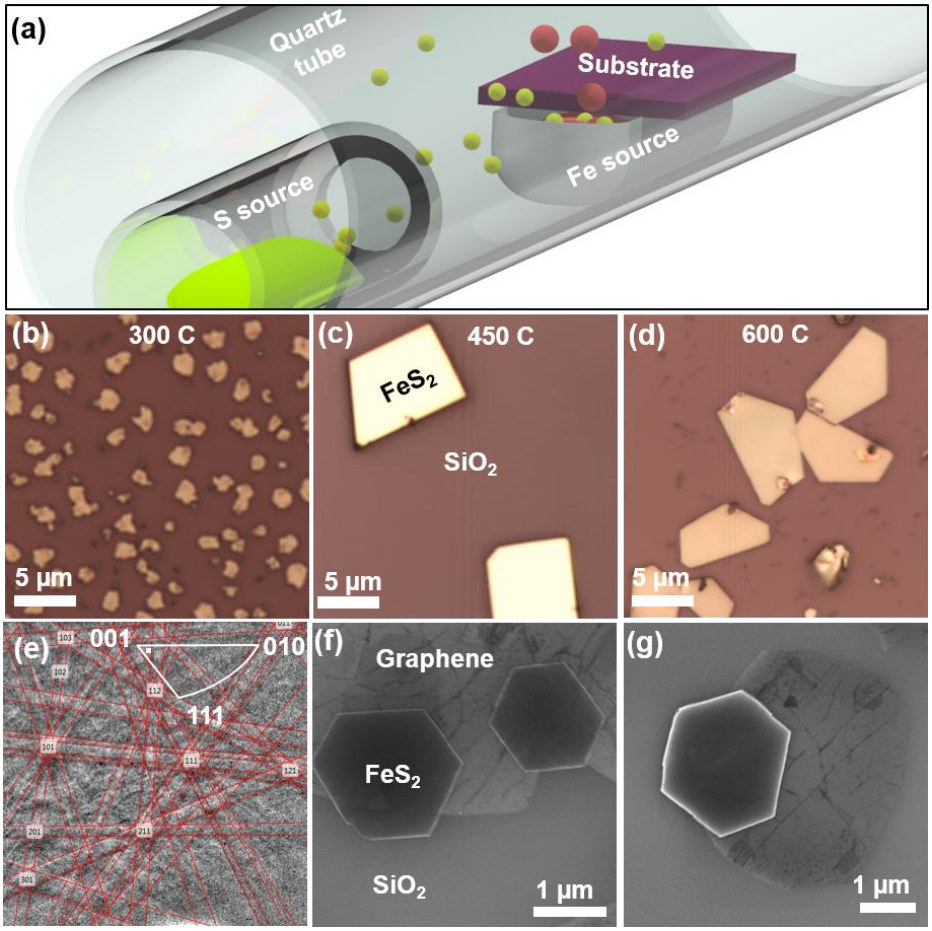

Figure 1. CVD growth, morphology, and structure of pyrite crystals. CVD set-up **(a)** used for the growth of the pyrite crystals. Optical images of the pyrite crystals grown at 300 C **(b)**, 450 C **(c)**, and 600 C **(d)**. A typical EBSD pattern **(e)** of the pyrite crystals grown at 450 C. The lower right inset shows the inverse pole figure. SEM images **(f** and **g)** of the pyrite crystals grown at 600 C on the graphene islands.

Computational methodology

We performed density functional theory (DFT) calculations using generalized gradient approximations (GGA) with Perdew-Burke-Ernzerhof (PBE) parametrization[31,32] for the exchange correlation functional, as implemented in the Vienna *Ab-initio* Simulation Package (VASP)[33,34], and with the pseudopotential provided with VASP. The atomic positions were optimized through the minimization of energy using Hellman-Feynman forces acting on atoms with the Broyden-Flecher-Goldfarb-Shanno (BFGS) scheme. The bulk pyrite was relaxed until the forces were less than 0.0001 eV/Å. A plane wave basis set with kinetic energy cut-off of 520 meV was used to expand the electronic wave functions, and an 8 × 8 × 8 Monkhorst Pack k-point mesh was adopted for the integration over the first Brillouin zone (BZ). In pyrite, the strong on-site Coulomb repulsion, arising from the narrow d-band of Fe, cannot be captured properly with spin-polarized DFT. The spurious self-interaction of electrons with its own charge introduces large error for localized states. Hence, to compensate the over-localization of Fe 3d state, we made use of Dudarev DFT+U method as implemented in VASP code[35], which combines DFT with a Hubbard Hamiltonian. As parameters of DFT+U (GGA+U), we used U = 2.0 eV[36,37] in the Collinear spin polarized calculation, which gives best agreement of the lattice constant (5.433 Å) with the experimental values (5.42 Å)[27,28]. The complete phonon dispersion along the BZ path was calculated for a 2x2x2 supercell and 3x3x3 k-point mesh, using finite displacement scheme implemented in Phonopy[39]. The displacement amplitude is 0.01 Å. The asymptotic long-range dipole-dipole interaction is included as a correction to the interatomic force constants, by calculating Born effective charge and dielectric tensor.

Results and Discussion

As a starting point, we investigated the role of the temperature in the growth of pyrite crystals, as detailed in Methods. The optical images show the pyrite crystals with different morphologies grown on the SiO_2 substrates at 300 C (**Figure 1b**), 450 C (**Figure 1c**), and 600 C (**Figure 1d**). At 300 C, the reactants form mainly small irregular-shaped crystals, which indicates an incomplete reaction. Increasing the temperature to 450 C promotes the formation of irregular trapezoidal crystals. Upon increasing the temperature to 600 C, well-defined 2D trapezoidal shaped crystals are obtained as the predominant product, similar to those reported for the SnS_2 growth in our previous work[40]. The results suggest that the morphology of the

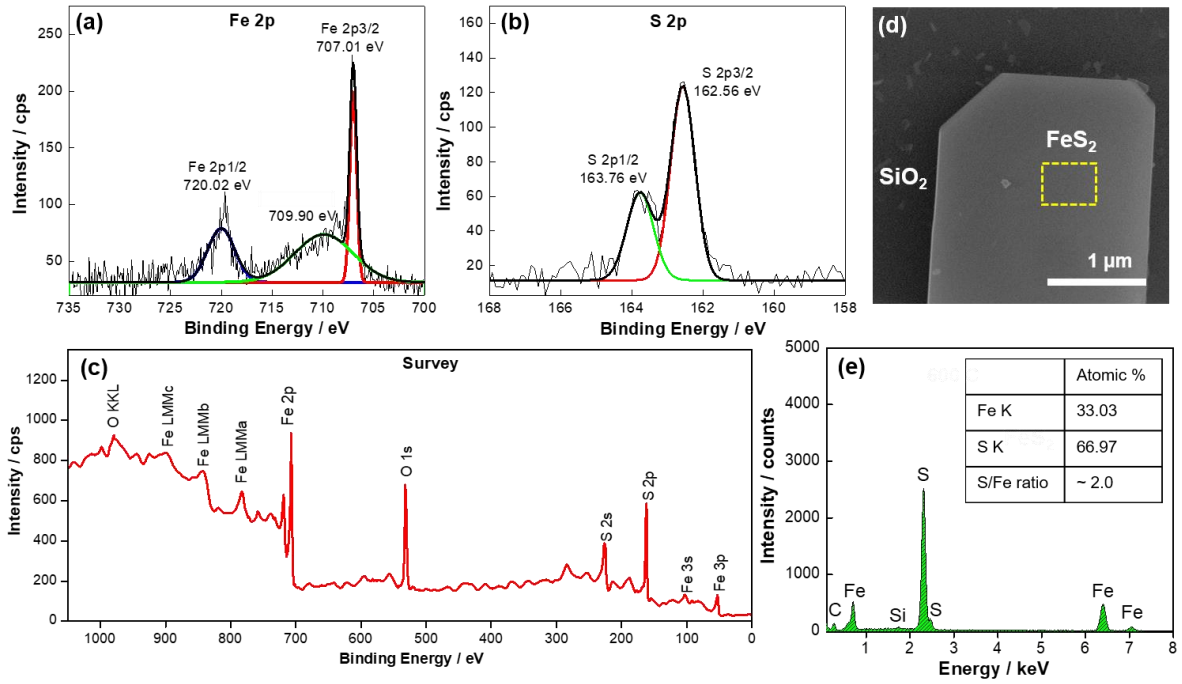

Figure 2. Surface chemistry, phase purity and chemical composition of pyrite crystals. High resolution XPS Fe 2p **(a)**, and S 2p **(b)** core level spectra, and XPS survey spectra **(c)** of the pyrite crystals grown at 450 C. SEM image **(d)** and corresponding EDS spectra **(e)** of the crystals grown at 450 C.

crystals is strongly dependent on the growth temperature. The anisotropic growth behavior of the crystals with various morphologies may originate from the crystalline facets, which tend to develop on the low-index planes to minimize the surface energy when growing. [41] For the growth at 450 C, EBSD analysis (**Figure 1e**) confirm the pyrite phase of the crystals with a preferred growth orientation along [001], which is considered as the most stable orientation for pyrite. [42,43]

To demonstrate the versatility and scalability of our method, we also grew the pyrite crystals on graphene/SiO_2 substrates using graphene islands as growth template, as described in Methods. SEM images (**Figure 1f** and **1g**) reveal that the crystals grown on the graphene islands are in the form of 2D hexagonal plates, while the growth on the bare SiO_2 promotes the formation of 2D trapezoidal shaped crystals at the same growth temperature (**Figure 1d**). Moreover, the pyrite crystals nucleate mostly at the edges of the graphene islands since the dangling bonds at the graphene edges are likely to attract to the reactants, and thus serving as nucleation sites.[44] Since the pyrite crystals prefer to grow onto the graphene islands instead of the bare SiO_2 substrate, this approach can be utilized for the patterned growth of pyrite for specific applications, or the heterostructures of pyrite and graphene may bring us novel magnetic properties promising for spintronic applications[45].

The surface chemistry of the crystals was studied using XPS measurements. Fe 2p core level spectra (**Figure 2a**) consist of two predominant peaks located at 707.01 eV, and 720.02 eV, respectively, corresponding to Fe $2p_{3/2}$ and Fe $2p_{1/2}$ spin-orbit doublets.[46] The binding energies (BEs) are in good agreement with the BEs of Fe in pyrite.[23,25] Fe $2p_{3/2}$ peak shows a high-energy tail at 709.90 eV, which is considered to be caused by slight Fe (III) - S or Fe (III) - O contamination of the surface.[23,47] Asymmetric S 2p spectra (**Figure 2b**) reveal two well-resolved S $2p_{3/2}$ and S $2p_{1/2}$ doublets with a spin orbit splitting of 1.2 eV.[23] The BEs of $2p_{3/2}$ and S $2p_{1/2}$ peaks are 162.56 eV, and 163.76 eV, respectively, which are consistent with those of S reported for pyrite.[21,25,48-50] No peaks associated with the impurity phases, such as marcasite or pyrrhotite, are observed.[51] Moreover, XPS survey scan (**Figure 2c**) shows no impurities or residues of the precursors.[46] The results confirm the growth of single-phase pyrite crystals with high purity at 450 C.

The chemical composition of the crystals was identified by EDS measurements. EDS spectra of the crystals grown at 450 C show only the presence of Fe and S. No contaminants were observed beside a negligible amount of C and Si. Quantitative EDS analysis reveal a S to Fe ratio of ~ 2.0. The results confirm the growth of the stoichiometric pyrite crystals with the high purity at 450 C. Fiechter et al.[52] reported that the pyrite crystals grown at ~ 575 C are deficient in sulfur. Hopfner et al.[53] reported that the deposition at the temperatures above 575 C yields sulfur deficient pyrite films. The pyrite crystals grown at 600 C in our study are thus expected to be deficient in sulfur.

Furthermore, we used Raman spectroscopy - a highly sensitive analytical technique for phase identification in iron sulfides[11,20,25,54] - to identify the phase of the crystals grown at different temperatures (**Figure 3a**). Raman spectra of a crystal grown at 450 C show three sharp peaks at 338.8 cm^{-1}, 375.5 cm^{-1}, and 424.4 cm^{-1}, corresponding to, respectively, E_g, A_g, and $T_g^{(3)}$ Raman active modes of pyrite.[2,55] The observed peaks match closely with *ab-initio* phonon calculation (**Figure 3b**) for the pyrite phase. There is no unstable phonon mode anywhere on the irreducible BZ in the phonon density of states (PDOS) (**Figure 3c**). A_g and $T_g^{(3)}$ phonon modes are attributed to in-phase and

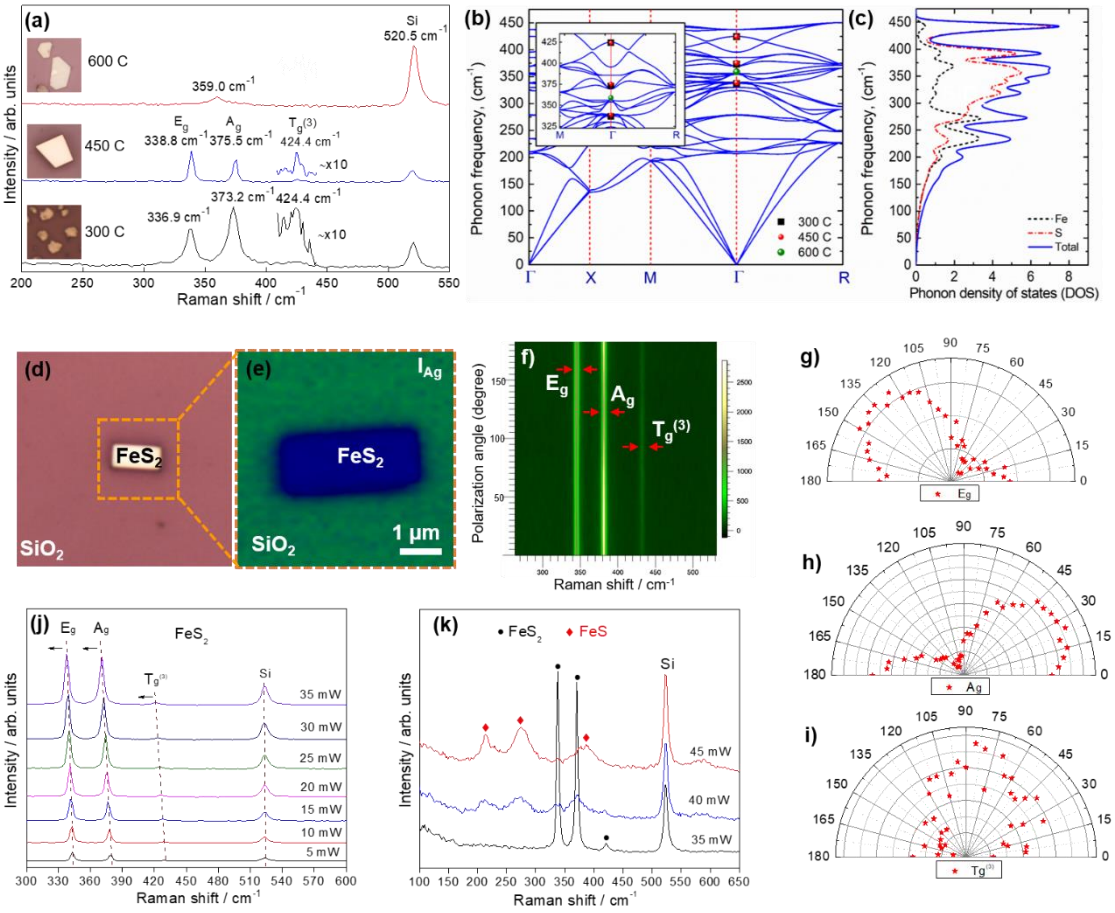

Figure 3. Raman spectroscopy and *ab-initio* calculations. Raman spectra comparison **(a)** of the crystals grown at 300 C, 450 C, and 600 C. Inset shows the optical images of the crystals used for Raman characterization. Calculated phonon dispersion **(b)** of pyrite. The symbols indicate the measured Raman peaks in **(a)**. PDOS **(c)**. The dash lines indicate the contribution from Fe and S atom vibration. Optical image **(d)** and corresponding Raman mapping **(e)** of a pyrite crystal grown at 450 C. 3D mapping **(f)** and the corresponding E_g **(g)**, A_g **(h)**, and $Tg^{(3)}$ **(i)** polar plots of Raman spectra with chancing the incident laser polarization angle from 0 to 180° for a pyrite crystal grown at 450 C. Evolution of Raman spectra of a typical pyrite crystal grown at 450 C recorded at different laser powers ranging from 5 to 35 mW **(j)**, and 35 to 45 mW **(k)**, with a 5 mW increment.

out-of-phase stretching vibrations of S_2 dumbbells, respectively, and S atoms are displaced perpendicular to S-S bond axis in E_g mode.[56,57] The PDOS (**Figure 3c**) also suggest that the optical modes beyond 275 cm^{-1} primarily involves the motion of S atom. These results are in good agreement with those of the previous studies on pyrite.[11,23,58] No impurity phases like marcasite are observed in Raman spectra, confirming the phase purity.[25] Raman mapping (**Figure 3d** and **3e**) further confirms the uniformity of the pyrite phase in the crystals. Two additional $Tg^{(1)}$ and $Tg^{(2)}$ modes of pyrite, which correspond to various combinations of librational and stretching motions[57], and are predicted to be Raman active by group theory[59], are not observed in the spectra since these weak peaks are probably concealed by strong E_g and A_g peaks.[5,25] ARPRS was utilized to identify these missing peaks. We observed a slight variation in the intensities of E_g (**Figure 3g**), A_g (**Figure 3h**), and $Tg^{(3)}$ (**Figure 3i**) peaks with changing polarization angle of the incident laser beam relative to the crystals; however, $Tg^{(1)}$ and $Tg^{(2)}$ peaks are still not resolved (**Figure 3f**), in agreement with a previous study[2].

Similar to the pyrite crystals grown at 450 C, only three characteristic E_g, A_g, and $T_g^{(3)}$ peaks are observed at 336.9 cm^{-1}, 373.2 cm^{-1}, and 424.4 cm^{-1}, respectively, for the crystals grown at 300 C (**Figure 3a**). However, the peaks are broader, indicating a lower degree of crystallinity.[60] In addition, E_g and A_g peaks are redshifted by ~1.8 cm^{-1} and ~2.3 cm^{-1}, respectively, while $T_g^{(3)}$ does not change. The redshift can be attributed to the change in its crystallinity.[60] The larger shift in A_g peak, as compared to that of E_g, is attributed to the faster softening of A_g phonon mode that involves purely the vibration of S_2 dumbbells, due to the weaker bond strength for S-S.[11] We have also found that the crystals grown at 300 C are less stable than the crystals grown at higher temperatures. After the prolonged air exposure, the pyrite crystals grown at 300 C were partially converted to the marcasite[25] as confirmed by the Raman spectroscopy (**Figure S1**).

In contrast to the crystals grown at 300 C and 450 C, no typical pyrite Raman peaks are observed in Raman spectra of the crystals grown at 600 C (**Figure 3a**). Instead, only a peak at 359 cm^{-1} is observed beside the substrate Si peak, which belongs to pyrite phase as confirmed by *ab-initio* phonon calculations (**Figure 3b**). Since all the observed peaks correspond to calculated phonon modes of pyrite phase, we can conclude that the growth up to 600 C does not include any other

phase than pyrite. The similar peak was reported for the 2D FeS_2 nanostructures obtained by hot injection method by Jasion et al.[16], suggesting that the thinness of the crystals may not allow for the more typical Raman active modes[61].

Laser annealing is broadly used for crystallization of amorphous the pyrite films or suppressing marcasite phase in the pyrite films.[58] The understanding of stability of the pyrite crystals upon laser annealing is thus practically important. Herein, we investigated the thermal stability of the pyrite crystals grown at 450 C by in-situ Raman measurements with a laser power ranging from 5 to 45 mW under ambient conditions. The three typical pyrite modes are preserved without the appearance of any impurity phases to up to a laser power of 35 mW (**Figure 3j**), revealing high thermal stability of the pyrite crystals. Nevertheless, the peak locations, intensities, and widths are significantly changed with increasing laser power (**Table S1**) due to the local heating effect of the laser[62]. It has been shown that laser heating results in the changes of the Raman bands for many materials, especially those that are opaque.[62] Since pyrite is opaque and has an optical absorption band in the wavelength region of 300-1200 nm, which encompasses the wavelength (532 nm) of the laser used in this study, this effect is expected to be relevant to pyrite.[62]

Further increase in the laser power to 40 mW, two new peaks at 211.48 and 273.32 cm^{-1} appear (**Figure 3k**), in addition to the weak pyrite peaks, which are the characteristics of poorly crystallized or nanophase FeS (troilite) phase[63], indicating the partial phase transformation of pyrite to troilite. Upon increasing the laser power to 45 mW, the pyrite peaks disappear and a new troilite peak appears at 381.29 cm^{-1}, in addition to two troilite peaks that become sharper, confirming the complete irreversible phase transformation from pyrite phase to troilitie.

Conclusion

In summary, we successfully demonstrated the first growth of pyrite crystals with controlled morphologies on SiO_2 and graphene/SiO_2 via a facile atmospheric pressure CVD method. We showed that the higher temperature CVD growth can provide highly crystalline and stable, pure-phase pyrite crystals with 2D trapezoid and hexagonal morphologies, and the growth up to 600 does not include any other phase of iron sulfides. In-situ Raman studies suggest that pyrite has high thermal stability while the laser irradiation can be used for the on-demand control of local phase transformations in pyrite. This study opens a new approach for scalable synthesis of pyrite with controlled morphologies and phases, and this approach can be further developed and adopted for the growth of the atomically thin pyrite crystals and their heterostructures with graphene that may bring us enhanced or novel properties.

Conflicts of interest

There are no conflicts to declare.

Acknowledgements

This work was made possible by support from C-SPIN, a funded center of STARnet, through a Semiconductor Research Corporation (SRC) program sponsored by MARCO and DARPA. This work used the Extreme Science and Engineering Discovery Environment (XSEDE), which is supported by the National Science Foundation (NSF) under the grant number ACI-1053575. SEM, EDS, and EBSD measurements were performed in the CFAMM at UC Riverside. XPS measurements were performed in the ACIF at the UC Riverside, which is supported by the NSF under the grant number DMR-0958796. Raman measurements were performed in the ACIF at UC Riverside. The authors would like to thank Dr. Andrew King for his assistance with the ARPRS measurements. The authors also would like to thank Mr. Jeffrey Bell for artistic contributions.

References

1 V. K. Gudelli, V. Kanchana, S. Appalakondaiah, G. Vaitheeswaran and M. C. Valsakumar, *J. Phys. Chem. C*, 2013, **117**, 41.
2 A. K. Kleppe and A. P. Jephcoat, *Mineral. Mag.*, 2004, **68**, 03.
3 A. Hung, I. Yarovsky, J. Muscat, S. Russo, I. Snook and R. O. Watts, *Surf. Sci.*,2002, **501**, 3.
4 M. Caban-Acevedo, N. S. Kaiser, C. R. English, D. Liang, B. J. Thompson, H.-E. Chen, K. J. Czech, J. C. Wright, R. J. Hamers, and S. Jin, *J. Am. Chem. Soc.*, 2014, **136**, 17163.
5 S. Shukla, G. Xing, H. Ge, R. R. Prabhakar, S. Mathew, Z. Su, V. Nalla, T. Venkatesan, N. Mathews, T. Sritharan, T. C. Sum and Q. Xiong, *ACS Nano*, 2016, **10**, 4.
6 S. Fiechter, J. Mai, A. Ennaoui and W. Szacki, *J. Cryst. Growth*, 1986, **78**,3.
7 Y. S. -Horn and Q. C. Horn, *Electrochim. Acta*, 2001, **46**, 17.
8 L. Xu, Y. Hu, H. Zhang, H. Jiang, and C. Li, *ACS Sustain. Chem. Eng.*, 2016, 4, 8.
9 L. Li, M. C. -Acevedo, S. N. Girard and S. Jin, *Nanoscale*, 2014, **6**, 4.
10 D. Liang, M. Cabán-Acevedo, N. S. Kaiser, and Song Jin, *Nano Lett.*, 2014, **14**, 12.
11 M. C -Acevedo, D. Liang, K. S. Chew, J. P. Degrave, N. S. Kaiser and S. Jin, *ACS Nano*, 2013, **7**, 2.
12 J. Puthussery, S. Seefeld, N. Berry, M. Gibbs and M. Law, *J. Am. Chem. Soc.*, 2011, **133**, 4.
13 M. C. -Acevedo, M. S. Faber, Y. Tan, R. J. Hamers and S. Jin, *Nano Lett.*, 2012, **12**, 4.
14 A. Kirkeminde, B. A. Ruzicka, R. Wang, S. Puna, H. Zhao and S. Ren, *ACS Appl. Mater. Interfaces*, 2012, **4**, 3.
15 H. A. MacPherson and C. R. Stoldt, *ACS Nano*, 2012, **6**, 10.
16 D. Jasion, J. M. Barforoush, Q. Qiao, Y. Zhu, S. Ren and K. C. Leonard, *ACS Catal.*, 2015, **5**, 11.
17 M. S. Faber, M. A. Lukowski, Q. Ding, N. S. Kaiser, and Song Jin, *J. Phys. Chem. C*, 2014, **118**, 37.
18 H. Zhang, Y. M. Dai and L. M. Liu, *Comput. Mater. Sci.*, 2015, **101**.
19 I. N. Yakovkin and N. V. Petrova, *Appl. Surf. Sci.*, 2016, **377**.
20 B. -B. Yu, X. Zhang, Y. Jiang, J. Liu, L. Gu, J. -S. Hu and L. -J. Wan, *J. Am. Chem. Soc.*, 2015, **137**, 6.
21 C. Wadia, Y. Wu, S. Gul, S. K. Volkman, J. Guo and A. P. Alivisatos, *Chem. Mater.,* 2009, **21**, 13.
22 M. A. A. Schoonen, and H.L.Barnes, *Geochim. Cosmochim. Acta*, 1991, **55**, 6.
23 S. Seefeld, M. Limpinsel, Y. Liu, N. Farhi, A. Weber, Y. Zhang, N. Berry, Y. J. Kwon, C. L. Perkins, J. C. Hemminger, R. Wu and M. Law, *J. Am. Chem. Soc.*, 2013, **135**, 11.
24 D.-Y. Wang, Y.-T. Jiang, C.-C. Lin, S.-S. Li, Y.-T. Wang, C.-C. Chen, C.-W. Chen, *Adv. Mater.*, 2012, **24**.

25 N. Berry, M. Cheng, C. L. Perkins, M. Limpinsel, J. C. Hemminger and M. Law, *Adv. Energy Mater.*, 2012, **9**.
26 L. Samad, M. C. -Acevedo, M. J. Shearer, K. Park, R. J. Hamers and S. Jin, *Chem. Mater.*, 2015, **27**, 8.
27 N. Takahashi, T. Yatomi and T. Nakamura, *Solid State Sci.*, 2004, **6**, 11.
28 N. Takahashi, T. Sawada, T. Nakamura and T. Nakamura, *J. Mater. Chem.*, 2000, **10**, 10.
29 S. Temiz, Z. Mutlu, S. Shahrezaei, M. Ozkan and C. S. Ozkan, *MRS Commun.*, 2017, **7**, 4.
30 D. A. Shirley, *Phys. Rev. B*, 1972, **5**, 12.
31 J. Perdew, K. Burke and M. Ernzerhof, *Phys. Rev. Lett.*, 1996, **77**, 18.
32 M. Ernzerhof and G. E. Scuseria, *J. Chem. Phys.*, 1999, **110**, 11.
33 [33G. Kresse and J. Hafner, *Phys. Rev. B*, 1993, **47**.
34 G. Kresse and J. Furthmüller, *Phys. Rev. B*, 1996, **54**, 16.
35 S. L. Dudarev, S. Y. Savrasov, C. J. Humphreys and A. P. Sutton, *Phys. Rev. B*, 1998, **57**, 3.
36 J. Hu, Y. Zhang, M. Law and R. Wu, *Phys. Rev. B - Condens. Matter Mater. Phys.*, 2012, **85**.
37 P. Xiao, X.-L. Fan, L.-M. Liu and W.-M. Lau, *Phys. Chem. Chem. Phys.*, **2014**, 16, 44.
38 B. X. Yuan, W. L. Luan, S. T. Tu and J. Wu, *New J. Chem.*, 2015, **39**, 5.
39 A. Togo and I. Tanaka, *Scr. Mater.*, 2015, 108.
40 Z. Mutlu, R. J. Wu, D. Wickramaratne, S. Shahrezaei, C. Liu, S. Temiz, A. Patalano, M. Ozkan, R. K. Lake, K. A. Mkhoyan and C. S. Ozkan, *Small*, 2016, **12**, 22.
41 J. Goebl, Q. Zhang, L. He and Y. Yin, *Angew. Chemie - Int. Ed.*, 2012, **51**, 2.
42 A. Hung, J. Muscat, I. Yarovsky and S. P. Russo, *Surf. Sci.*, 2002, **513**, 3.
43 A. S. Barnard and S. P. Russo, *J. Mater. Chem.*, 2009, **19**, 21.
44 M. Liu, Y. Li, P. Chen, J. Sun, D. Ma, Q. Li, T. Gao, Y. Gao, Z. Cheng, X. Qiu, Y. Fang, Y. Zhang and Z. Liu, *Nano Lett.*, 2014, **14**, 11.
45 W. Han, R. K. Kawakami, M. Gmitra and J. Fabian, *Nat. Nanotechnol.*, 2014, **9**, 10.
46 A. P. Grosvenor, B. A. Kobe, M. C. Biesinger and N. S. McIntyre, *Surf. Interface Anal.*, 2004, **36**, 12.
47 H. W. Nesbitt and I. J. Muir, *Geochim. Cosmochim. Acta*, 1994, **58**, 21.
48 A. Ennaoui, *J. Electrochem. Soc.*, 1986, **133**, 1.
49 G. Smesta, A. Ennaoui, S. Fiechter, H. Tributsch, W. K. Hofmann, M. Birkholz and W. Kautek, *Sol. Energy Mater.*, 1990, **20**, 3.
50 S. Chaturvedi, R. Katz, J. Guevremont, M. A. A. Schoonen and D. R. Strongin, *Am. Mineral.*, 1996, **81**, 1-2.
51 A. R. Lennie and D. J. Vaughan, *Miner. Spectrosc. a Tribut. to Roger G. Burn.*, 1996, **5**.
52 S. Fiechter, M. Birkholz, A. Hartmann, P. Dulski, M. Giersig, H. Tributsch and R.J.D. Tilley, *J. Mater. Res.*, 1992, **7**, 7.
53 C. Höpfner, K. Ellmer, A. Ennaoui, C. Pettenkofer, S. Fiechter and H. Tributsch, *J. Cryst. Growth*, 1995, **151**, 3-4.
54 A. K. Kleppe and A. P. Jephcoat, Mineral. Mag., 2004, 68, 3.
55 H. Vogt, T. Chattopadhyay and H. J. Stolz, *J. Phys. Chem. Solids*, 1983, **44**, 9.
56 C. De Las Heras, J. L. Martín De Vidales, I. J. Ferrer and C. Sánchez, *J. Mater. Res.*, 1996, **11**.
57 C. Sourisseau, R. Cavagnat and M. Fouassier, *J. Phys. Chem. Solids*, 1991, **52**, 3.
58 M. Umehara, Y. Takeda, H. Azuma, and T. Motohiro, International Conference on Solid State Devices and Materials, 2011.
59 S. Ushioda, *Solid State Commun.*, 1972, **10**, 3.
60 G. Viera, S. Huet and L. Boufendi, *J. Appl. Phys.*, 2001, **90**, 8.
61 X. Luo, Y. Zhao, J. Zhang, M. Toh, C. Kloc, Q. Xiong and S. Ying Quek, *Phys. Rev. B - Condens. Matter Mater. Phys.*, 2013, **88**, 19.
62 R. N. Bryant, J. D. Pasteris, D. A. Fike, *Appl. Spectrosc*, 2018, **72**, 1.
63 B. Mao, Q. Dong, C. L. Exstrom and J. Huang, *Thin Solid Films*, 2014, **562**.

Chemical Vapor Deposition and Phase Stability of Pyrite on SiO_2

Chemical vapor deposition and phase stability of pyrite crystals on SiO_2 at temperatures up to 600 C have been studied.